Advances in Aircraft and Spacecraft Science, *Vol. 7, No. 5 (2020) 425-440*
DOI: https://doi.org/10.12989/aas.2020.7.5.425

Numerical investigation for performance prediction of gas dynamic resonant igniters

Antonietta Conte[a], Andrea Ferrero[b] and Dario Pastrone*

DIMEAS, Politecnico di Torino, Corso Duca degli Abruzzi 24, 10129 Torino, Italy

(Received January 7, 2020, Revised May 15, 2020, Accepted May 18, 2020)

Abstract. The work presented herein is a numerical investigation of the flow field inside a resonant igniter, with the aim of predicting the performances in terms of cavity temperature and noise spectrum. A resonance ignition system represens an attractive solution for the ignition of liquid rocket engines in space missions which require multiple engine re-ignitions, like for example debris removal. Furthermore, the current trend in avoiding toxic propellants leads to the adoption of green propellant which does not show hypergolic properties and so the presence of a reliable ignition system becomes fundamental. Resonant igniters are attractive for in-space thrusters due to the low weight and the absence of an electric power source. However, their performances are strongly influenced by several geometrical and environmental parameters. This motivates the study proposed in this work in which the flow field inside a resonant igniter is numerically investigated. The unsteady compressible Reynolds Averaged Navier-Stokes equations are solved by means of a finite volume scheme and the effects of several wall boundary conditions are investigated (adiabatic, isothermal, radiating). The results are compared with some available experimental data in terms of cavity temperature and noise spectrum.

Keywords: resonant igniter; liquid rocket engine; CFD; boundary conditions

1. Introduction

Hartmann (1922) showed that an under-expanded gas jet can produce high intensity wave oscillations if the jet is made to interact with a cavity. The phenomenon is influenced by several parameters: nozzle diameter, nozzle-cavity opening distance (i.e. s/d the ratio between jet nozzle exit distance from cavity inlet s and nozzle exit diameter d), cavity geometry (form, diameter, length), thermodynamic properties of the operating gas, tube material, wall friction, nozzle pressure ratio (NPR). The cavity walls can rapidly reach high temperatures when the interaction with the under-expanded gas jet leads to resonance phenomena. Depending on the design parameters of the resonator, the temperature in the cavity can be far higher than the gas jet stagnation temperature (Sprenger 1954). These phenomena are of great interest in rocketry, since the temperature growth can be exploited for achieving the ignition of liquid propellant engines. Even though the resonant igniter concept is not new, some commercial attempts to design and

*Corresponding author, Professor, E-mail: dario.pastrone@polito.it
[a]Ph.D. Student, E-mail: antonietta.conte@polito.it
[b]Assistant Professor, E-mail: andrea_ferrero@polito.it

http://www.techno-press.org/?journal=aas&subpage=7 ISSN: 2287-528X (Print), 2287-5271 (Online)

produce devices for space applications have been made recently.

According to EU REACH regulations, there is a growing trend in the use of green propellants which could substitute toxic and carcinogenic materials, such as hydrazine and its derivatives (ECHA 2011a, b). Several historical liquid propellants, like hydrazine and its derivatives, are widely used because of their reliability and some interesting properties, like for example the ability to spontaneously ignite (hypergolic propellants) which is particularly desirable for space missions during which several re-ignitions are required (for example for debris removal missions). However, the use of hypergolic propellants is risky as shown by numerous incidents during the long history of hydrazine-derived propellant (Nufer 2010). Green propellants lack the hypergolic properties and so they require a reliable ignition system.

Several technologies are available for the ignition of liquid rocket engines. The electrical spark has been proven to be the safest, most reliable and widely used method of igniting a combustor, e.g., by adopting internal combustion engine sparkplugs. However, electric ignition adds complexity, requires electrical power and a high-voltage electrical source. It is also susceptible to electromagnetic damage. An example of traditional igniter system is the one adopted for the Ariane 6 upper stage engine Vinci, which uses a torch igniter fed from dedicated high-pressure tanks capable of ensuring re-ignitability (Frenken *et al.* 2002). Another approach is represented by the Falcon 9 developed by SpaceX which uses a combination of TEA/TEB for the ignition of the first and second stages. The TEA/TEB combination is pyrophoric, igniting spontaneously on contact with air. This pose handling issues and requires careful treatment, since pollution of the igniter feed lines can cause launch abort.

In this framework, a simple, highly reliable and lightweight alternative is represented by the resonant igniter which is based on a sonic/supersonic nozzle which ejects a jet in front of a cavity. This technology does not require movable parts, electrical systems or external power supplies. These advantages are important for long missions, where a high number of ignitions are required. A large number of prototypes with different propellants combination have been tested in the past for various propellant combination (Stanbisky *et al.* 2005, Song *et al.* 2005, Kessaev *et al.* 2001), but none of them have been adopted as flight hardware due to the dependence of s/d (nozzle-resonance cavity opening distance) for optimal resonant heating from the nozzle pressure ratio (NPR). It has been demonstrated that it is possible to expand the spectrum of s/d for optimal resonant heating considering specific designs of inlet nozzle geometries (Brocher *et al.* 1983, Schmidt *et al.* 2015).

An acoustic igniter has two main operating modes when the nozzle pressure ratio is increased beyond a critical limit: the Jet Regurgitant Mode (JRM) and the Jet Screech Mode (JSM). The JRM is characterized by an inflow phase, where the jet stream enters the cavity and travels inside the cavity towards the closed end. If the cavity is long enough, the waves coalesce to a single shockwave which is reflected at the closed end and travel towards the opening. The gas leaves the cavity and displaces the free stream jet; the cavity is emptied, and a new cycle starts. Under certain conditions, a small fraction of the resonance gas can remain inside the cavity, causing gradual heating due to irreversible phenomena and the gas temperatures can increase to a value beyond the stagnation temperature at the closed end of the resonator.

The JSM is characterized by an almost normal shock oscillating at high frequencies. Depending upon the geometrical parameters and flow parameters, both the JRM and JSM modes can be observed. Extensive fine-tuning of various parameters is required to initiate and maintain the resonance conditions required for heat generation. In this study, numerical simulations are performed to investigate the gas-dynamic oscillatory phenomena which govern the behavior of the

igniter. Care is here devoted to the choice of the thermal boundary conditions on the cavity wall in order to understand how these effects influence the performances of the igniter.

The simulations are performed by means of Unsteady Reynolds-averaged Navier-Stokes (URANS) simulations: this modelling choice is in line with previous works in the literature (see for example Bauer *et al.* (2019)) and it allows to perform a parametric study by capturing the main physical phenomena with a reasonable computational cost.

These investigations can give the physical insight required to drive the development of better igniters.

2. Reference design

A resonant igniter is made of a sonic or a supersonic nozzle and a resonant cavity. The gas is accelerated through the nozzle and an under-expanded jet is expelled into the surrounding environment. The resonant cavity is placed in front of the nozzle exit. Numerical investigations have been performed considering a conical cavity design made by Bauer *et al.* (2014). An example of this device is reported in Fig. 1 where the following geometrical parameters are defined according to the design considered by Bauer *et al.* (2014): nozzle exit diameter d = 5mm, cavity inlet diameter (D) -nozzle exit diameter (d) ratio D/d = 1.25, cavity base diameter (D1) - cavity inlet diameter (D) ratio D1/D=0.24, nozzle cavity gap (s) - nozzle exit diameter (d) ratio s/d=2.4, cavity depth (L) - cavity inlet diameter (D) ratio : L/D=11. This configuration was numerically and experimentally tested by Bauer *et al.* (2014). The resonators were installed in a vacuum chamber in order to reduce the heat flux from the cavity wall to the surrounding environment. The resonator closed end temperature was determined with thermocouples and the acoustic measurements were analyzed with a microphone. The results obtained from the work of Bauer *et al.* (2014) are reported in Fig. 2. The experimental campaign was conducted to find the optimum nozzle-cavity distance to obtain the maximum temperature, at fixed NPR=4. As previously mentioned, resonant heating performance depend on a number of factors including gas properties (e.g., heat capacity and molar mass) (Bauer *et al.* 2014). It was found that the highest obtainable temperature using air is achieved for s/d= 2.4, under the abovementioned conditions.

The microphone response spectrum indicates an intense heating, accompanied with distinct high amplitude screeching at 1.963 kHz (Bauer *et al.* 2014). The resonance heating phenomenon are very complex, and it is not possible to find a representative analytical solution, so computational fluid dynamics analyses are needed. This reference configuration is used in the present numerical study as a representative test case.

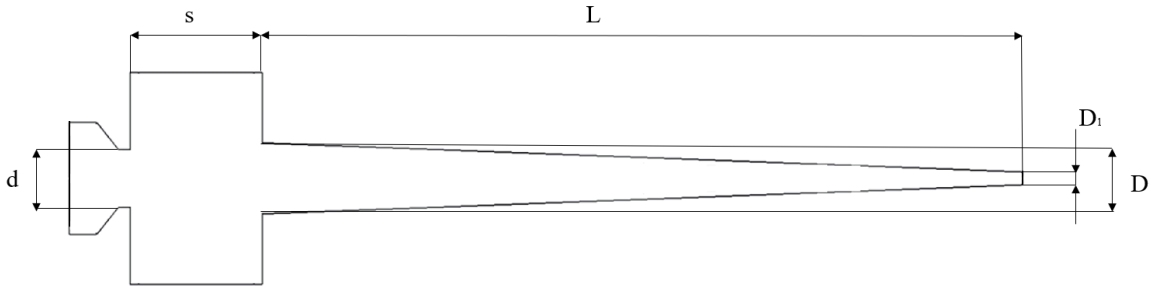

Fig. 1 Conical cavity design following the nomenclature of Bauer *et al.* (2014)

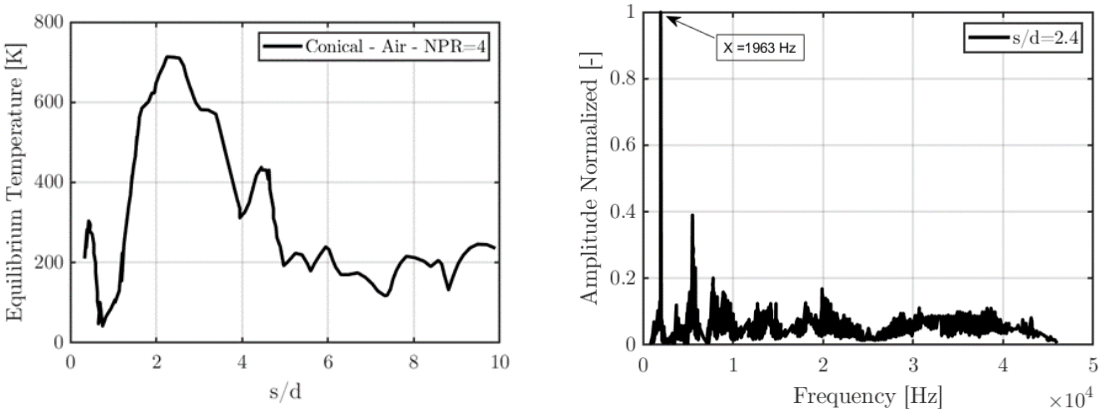

(a) Equilibrium temperature. (b) Microphone response spectrum.

Fig. 2 Equilibrium temperature for various nozzle distances at a NPR of 4. Microphone response spectrum for conical resonator at NPR 4 and s/d of 2.4 Data derived from the work of Bauer *et al.* (2014)

2.1 Physical model

The flow field inside the igniter is described in this study by the axisymmetric compressible Reynolds Averaged Navier-Stokes (RANS) equations. The Spalart-Allmaras model is adopted for turbulence closure. The governing equations are reported in the following:

$$\frac{\partial \rho r}{\partial t} + \nabla \cdot (\rho \boldsymbol{u} r) = 0 \tag{1}$$

$$\frac{\partial \rho \boldsymbol{u} r}{\partial t} + \nabla \cdot \left((\rho \boldsymbol{u}\boldsymbol{u} + p\boldsymbol{I} - \boldsymbol{\tau}) r \right) = \boldsymbol{s} \tag{2}$$

$$\frac{\partial E r}{\partial t} + \nabla \cdot \left(r(\boldsymbol{u}(p+E) - \boldsymbol{\tau} \cdot \boldsymbol{u} + \boldsymbol{q}) \right) = 0 \tag{3}$$

$$\frac{\partial \rho \tilde{\nu} r}{\partial t} + \nabla \cdot (r \rho \boldsymbol{u} \tilde{\nu}) = \rho r (P - D) \; + \frac{1}{\sigma} \nabla \cdot (\rho r (\nu + \tilde{\nu}) \nabla \tilde{\nu}) + \frac{c_{b2}}{\sigma} \rho r (\nabla \tilde{\nu})^2 - \frac{1}{\sigma} r (\nu + \tilde{\nu}) \nabla \rho \cdot \nabla \tilde{\nu} \tag{4}$$

where ρ, $\boldsymbol{u}$, E, $\tilde{\nu}$, p, r, $\boldsymbol{I}$, $\boldsymbol{s}$ represent density, velocity, total energy per unit volume, modified eddy viscosity, pressure, radius, identity matrix and axisymmetric source term, respectively. The source terms, P and D, and the model constants c_{b2} and σ are defined by Spalart and Allmaras (1994). The heat flux $\boldsymbol{q}$ is computed by means of the Fourier law:

$$\boldsymbol{q} = -c_p \left(\frac{\mu}{Pr} + \frac{\mu_t}{Pr_t} \right) \nabla T$$

where c_p, μ, μ_t, ∇T, $Pr = 0.72$ and $Pr_t = 0.9$ represent the constant pressure specific heat, the molecular dynamic viscosity, the turbulent eddy viscosity, the temperature gradient, the Prandtl number and the turbulent Prandtl number, respectively. The stress tensor $\boldsymbol{\tau}$ is evaluated following the Boussinesq hypothesis and contains both the viscous and turbulent contributions. More details on the axisymmetric form of the RANS equations can be found in the work of Bassi *et al.* (2011).

2.2 Space and time discretization

The governing equations are discretized by means of a parallel Fortran 90 solver which has been tested in both inviscid and viscous test cases (Ferrero and Larocca 2016, Ampellio *et al.* 2016, Ferrero *et al.* 2017, Ferrero and Larocca 2017). The solver allows to discretize the equations in space by means of the Finite Volume (FV) approach or the Discontinuous Galerkin (DG) approach. Both schemes lead to discontinuous solutions at the interfaces between the elements which can be exploited to define Riemann problems and compute the convective fluxes with an upwind approach. While in FV schemes the reconstruction is performed using the information from the neighboring cells, in DG schemes the reconstruction is based on the internal degrees of freedom of the elements. This makes the implementation of high-order schemes on unstructured meshes simpler for DG schemes with respect to FV schemes. However, the problem under study is characterized by the presence of shock waves which limit the accuracy order of the solution and hide several advantages of high-order schemes. A discussion on the use of FV and DG schemes for problems dominated by shock waves can be found in the work by Conte *et al.* (2019).

For this reason, the FV approach is used in this work. A second order accurate FV scheme is adopted due to its robustness and accuracy. The convective fluxes are computed by performing a limited reconstruction and then adopting the AUSM+ numerical flux by Liou (1996) at the interfaces. The limiting is performed following the approach of Barth and Jespersen (1989). The gradients required by the diffusive fluxes at the interfaces and by the source terms are computed by means of the weighted least square approach.

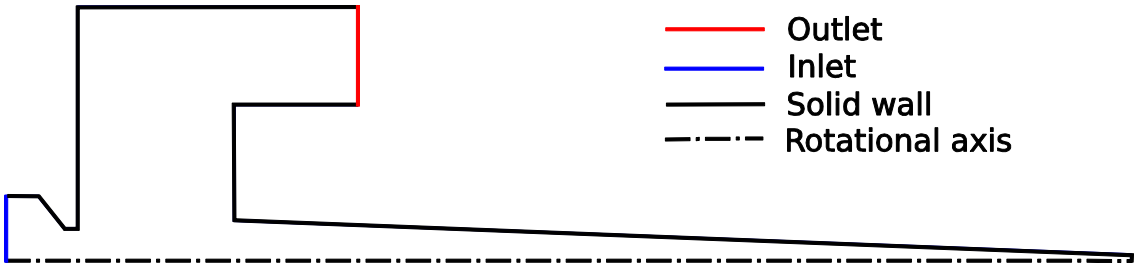

Fig. 3 Computational domain

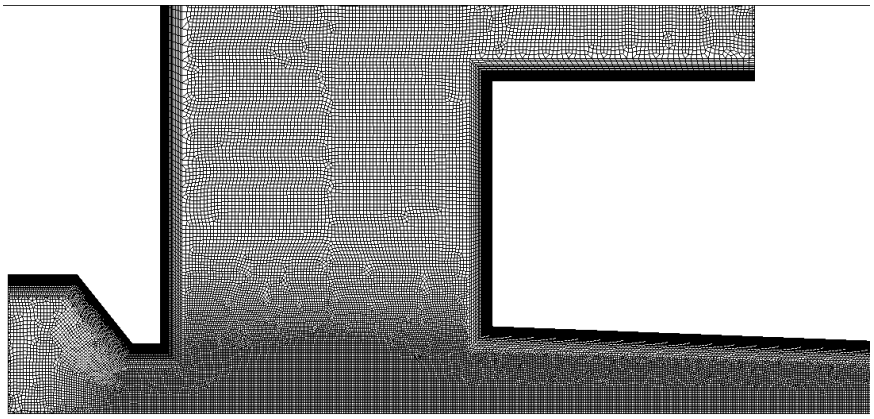

Fig. 4 Detail of coarse mesh in the region between nozzle exit and cavity inlet

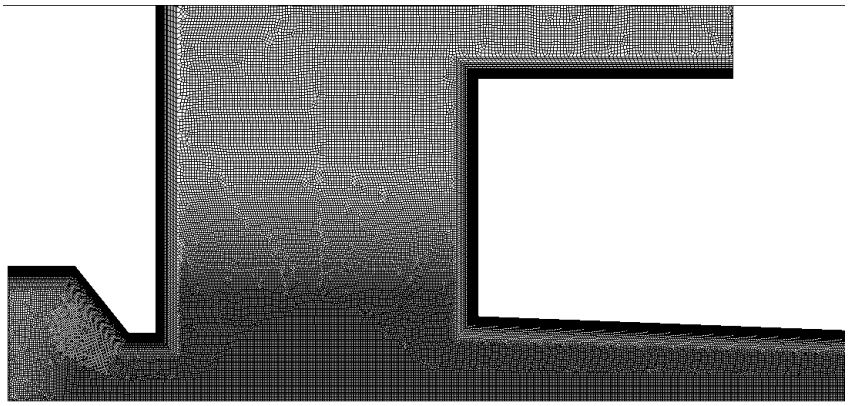

Fig. 5 Detail of medium mesh in the region between nozzle exit and cavity inlet

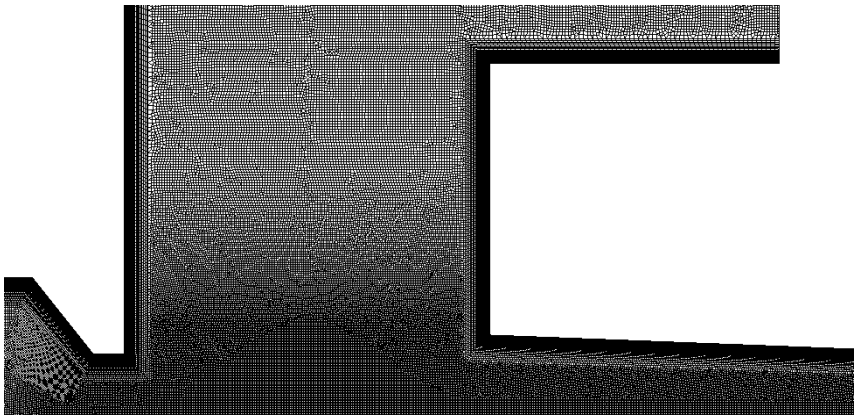

Fig. 6 Detail of the fine mesh in the region between nozzle exit and cavity inlet

Time integration is performed by means of a second order accurate linearized Crank-Nicholson method. The Jacobian matrix required by the implicit scheme is obtained numerically. The linear system resulting from the implicit discretization is solved in parallel by means of the iterative GMRES solver with the Additive Schwarz preconditioner. The solver is provided by the PETSc library (Balay *et al.* 2019).

The management of the mesh in the parallel environment is performed through the DMPlex class (Lange *et al.* 2015) provided by the PETSc library (Balay *et al.* 2019).

The computational domain is discretised by a mixed structured-unstructured mesh generated by the Gmsh tool of Geuzaine and Remacle (2009). In particular, the Frontal-Delaunay for quads algorithm by Remacle *et al.* (2013) is adopted. The computational domain is reported in Fig. 3 which shows the converging nozzle (on the left) and the cavity (on the right).

2.3 Boundary conditions

The working principle behind the resonant igniter is related to the entrapment of energy in the cavity: the fluid ejected by the nozzle transport energy and a fraction of this energy remains in the cavity, producing local heating. However, the heating of the fluid in the cavity activates several

mechanisms which could hide this phenomenon. In particular, the fluid in the cavity can release heat to the wall. For this reason, a study with several boundary conditions is performed in this work. First of all, an adiabatic boundary condition is considered for the solid wall. This represents the ideal boundary condition which allows to reach the maximum temperature in the cavity. This is in line with the experimental results of Sprenger (1954) who recommended the use of an insulating material for the cavity in order to remove heat losses through the wall.

Whilst the adiabatic boundary would represent the best choice for a resonant igniter, an isothermal boundary condition is also investigated in this work. In particular, an isothermal boundary condition with a wall temperature equal to the stagnation temperature of the jet is considered (Tw=300 K). This temperature is assumed equal to the environment temperature. This represents a very conservative assumption because it assumes that the wall remains cool and removes a significant amount of heat from the fluid in the cavity. Since the actual resonator will not have a perfectly adiabatic wall but not even a perfectly cooled wall, the simulations performed with these boundary conditions should represent the extreme working range that we could expect for this device.

Finally, a more reasonable boundary condition is adopted by assuming that the cavity wall is very thin. If the wall is thin, then the conduction across the cavity wall in the axial direction is negligible. However, when the fluid (and the wall which is contact to the fluid) reaches high temperatures, radiation effects could become not negligible. In particular, the heat propagates across the cavity wall and then it is radiated in the external environment. Furthermore, if the cavity wall is sufficiently thin it could be assumed that the temperature is constant through the wall thickness and so the power irradiated by the external surface of the device can be estimated by the Stefan-Boltzmann law computed with the fluid temperature at wall (T_w). In particular, the heat flux which is removed by the fluid and radiated in the external environment is computed as:

$$q_w = \epsilon \theta_{SB} T_w^4 \tag{5}$$

where ϵ and θ_{SB} represent the emissivity of the body (here set to 1) and the Stefan-Boltzmann constant ($\theta_{SB} = 5.67 \cdot 10^{-8}\ W/\ m^2K^4$).

2.4 Characteristic time for normalization of the results

The timescale of the problem has to be estimated in order to choose the timestep for the simulation. Convection in the fluid and conduction in the walls have different timescale and both phenomena are involved when resonance heating occurs. If the walls are considered adiabatic, only the convective timescale is taken into account. Bauer *et al.* (2019) demonstrated that a tapered resonator, has lower frequencies than the one evaluated with the linear acoustic theory. The behavior seems to be close to those of a cylindrical $\lambda/4$ resonator with an additional end correction.

The experimental fundamental frequency was chosen as a reference. The value $f_0 = 1963$ Hz is deduced from the experiments conducted by Bauer *et al.* (2014) and the convective timescale $\tau_{conv} = 1/f_0 =$ 0.51 ms is obtained. This timescale is used in the following to express the results in terms of normalised time $\vartheta = t/\tau_{conv}$.

3. Convergence analysis

First of all a convergence analysis is performed in order to quantify the discretization error. The

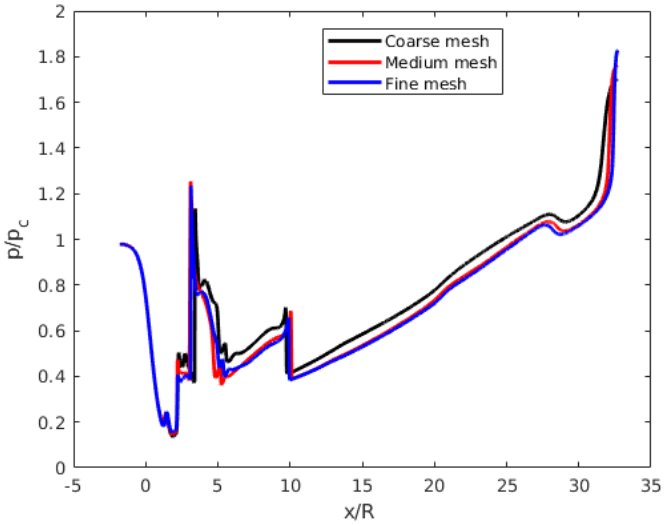

Fig. 7 Axial pressure distribution at $\theta = 1.5$ with different meshes

study is performed by checking the axial pressure distribution at the time $\vartheta = 1.5$ and repeating the simulation with different mesh resolutions. This approach follows the numerical study performed by Bauer *et al.* (2019), in which the grid convergence is assessed by checking the instantaneous pressure distribution after a finite time from the starting of the simulation.

The simulations are initialized by assuming a uniform field in the cavity and in the external region where the fluid is at rest and the pressure is equal to the environmental value (1 bar) while the total pressure in the converging portion of the nozzle is set to the tank value (4 bar).

This generates a shock wave which travels in the cavity and is reflected by the end wall. Several additional shocks are generated by the interaction with the other solid walls in the domain. The simulations are carried out with a CFL number equal to 25 and are performed on three different meshes with 99289, 145911 and 199785 cells, respectively. A picture of the meshes is reported in Figs. 4, 5 and 6. The instantaneous axial pressure distribution at $\vartheta = 1.5$ for the different meshes is reported in Fig. 7. The results show that the solution changes slightly when the medium and the fine meshes are considered and so all the following simulations are performed with the finest mesh resolution tested in this preliminary study.

4. Results

Several numerical simulations were conducted to analyze the oscillatory behavior inside the resonance cavity with the goal of understanding the sensitivity of the results with respect to the wall boundary condition.

A first set of simulations was performed with the adiabatic wall boundary conditions and the finest mesh. The goal of this first test is the qualitative investigation of the structures in the flow field. An instantaneous snapshot of the Mach field is reported in Fig. 8, in which a normal shock in front of the cavity is clearly visible. Two different snapshots of the pressure field during an oscillatory cycle are reported in Figs. 9 and 10 which show the large pressure variation at the end of the cavity.

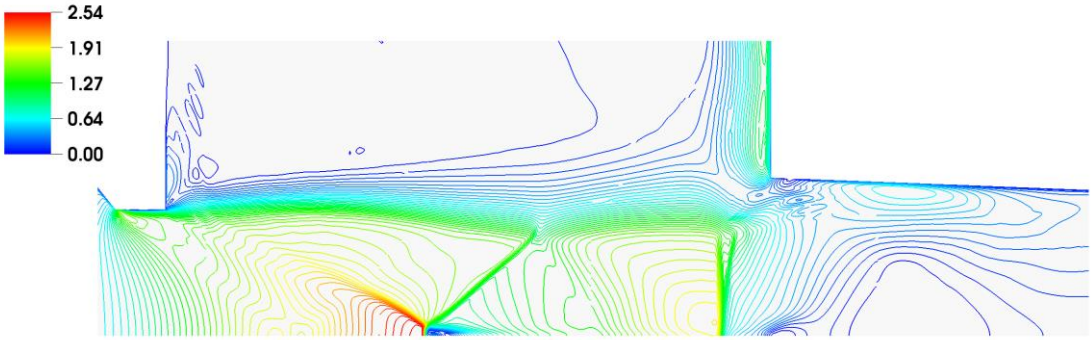

Fig. 8 Instantaneous Mach field in the area between the nozzle exit and the cavity inlet

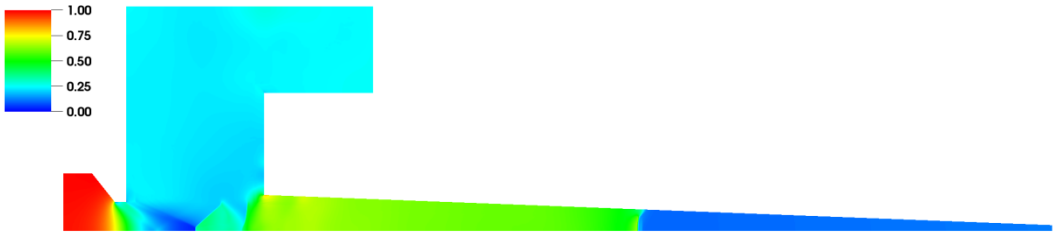

Fig. 9 Pressure field during an oscillatory cycle at time t1

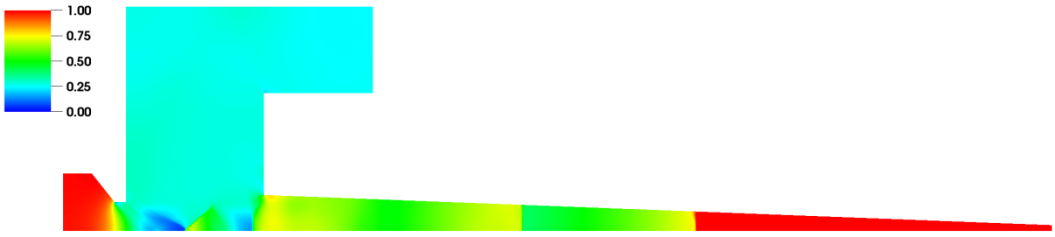

Fig. 10 Pressure field during an oscillatory cycle at time t2>t1

The simulations are repeated with the three boundary conditions discussed in Section 3.3. The time history of the cavity base temperature and the normalised static pressure are reported in Fig. 11. The cavity base temperature is here defined as the temperature measured in the fluid by a numerical probe located at 99% of the cavity length. The static pressure is evaluated in the same point and it is normalised with respect to the nozzle total pressure. In order to evaluate the average temperature in the cavity a moving average operator is applied to the temperature and pressure signals. The results are reported in Figs. 12, 13 and 14 for different amplitudes of the sliding window ($\Delta = \theta_{max}, \theta_{max}/2$ and $\theta_{max}/4$, , with $\theta_{max} = 24$). These plots allows to quantify the influence of the time window size: the same trend is observed in the three figures independently from the size of the time window used for the averaging operation.

The plot in Fig. 11(a) shows that the pressure at the end of the cavity strongly oscillates but there are no significant differences in the average value or in the oscillation amplitude between the different choices of boundary conditions. In contrast, the temperature history reported in

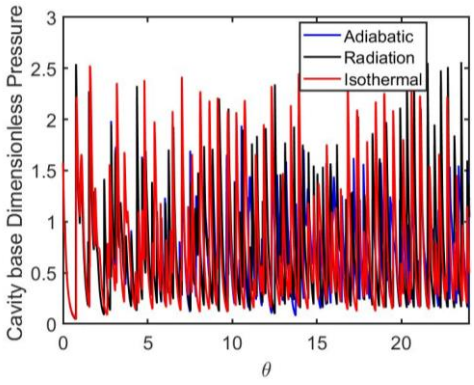

(a) Cavity base dimensionless pressure as a function of the dimensionless time

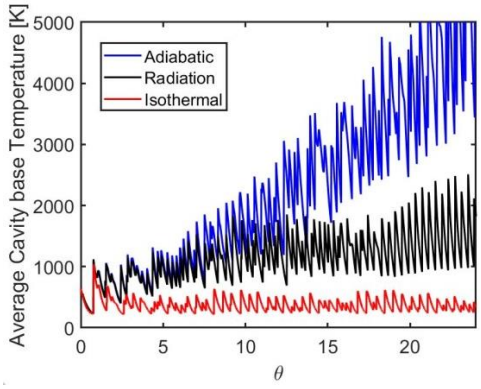

(b) Cavity base temperature as a function of dimensionless time

Fig. 11 Comparison between results obtained with adiabatic, radiation and isothermal boundary conditions

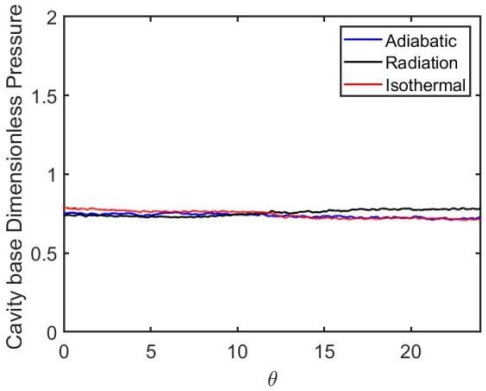

(a) Cavity base dimensionless pressure as a function of dimensionless time

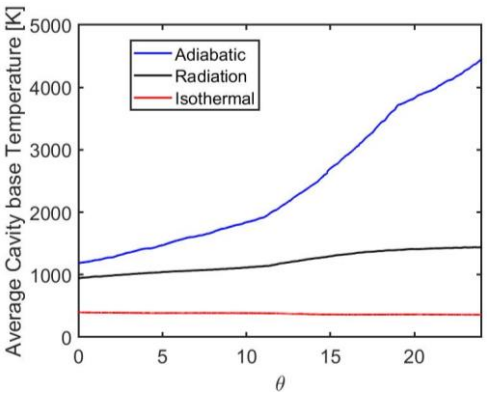

(b) Cavity base temperature as a function of dimensionless time

Fig. 12 Average temperature and pressure results obtained with different boundary conditions and an averaging time window size $\Delta = \theta_{max}$, with $\theta_{max} = 24$

Fig. 11(b) shows a strong dependency on the boundary condition. The results obtained by the adiabatic simulation are characterized by a diverging signal which exceeds 5000 K for $\theta > 24$. This is due to the fact that the heat accumulated in the cavity cannot escape across the solid wall but can only propagate through diffusion in the fluid. Also convection by mass transfer cannot remove heat from the end of the cavity since the portion of fluid at the end of the cavity is compressed and expanded but does not leave the cavity. For these reasons, the temperature at the end of the cavity increases quickly. The simulation was stopped at $\theta = 24$ because the temperature reached a value which is significantly higher than the experimental results provided by Bauer *et al.* (2014) for this configuration. Furthermore, the present simulations are performed by assuming an ideal gas with frozen chemical composition. When the temperature becomes so high the molecules start to dissociate and this represents another physical mechanism which can limit the temperature growth because the heat is used not just to increase the temperature but also

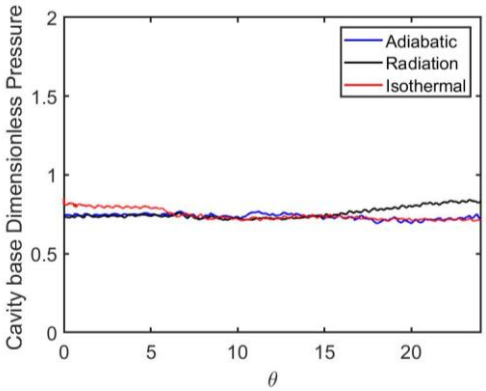

(a) Cavity base dimensionless pressure as a function of dimensionless time

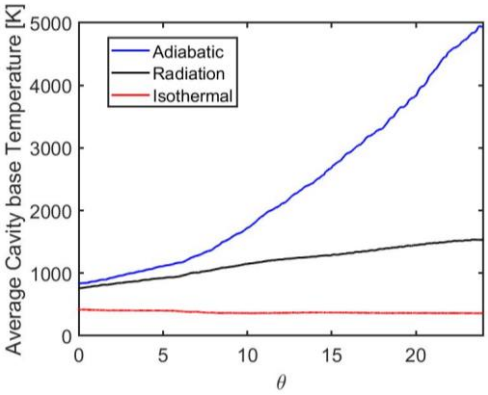

(b) Cavity base temperature as a function of dimensionless time

Fig. 13 Average temperature and pressure results obtained with different boundary conditions and an averaging time window size $\Delta = \theta_{max}/2$, with $\theta_{max} = 24$

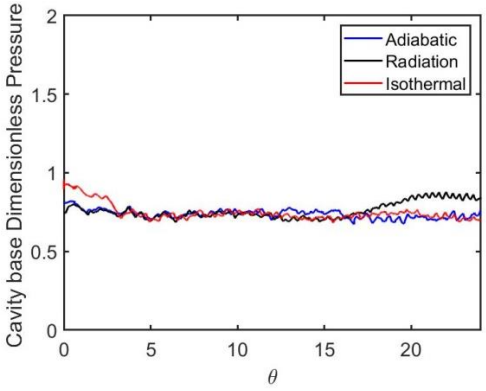

(a) Cavity base dimensionless pressure as a function of dimensionless time

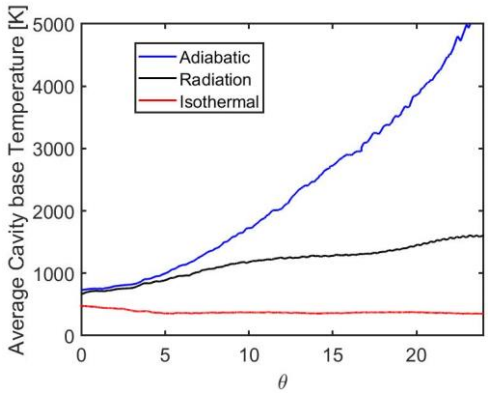

(b) Cavity base temperature as a function of dimensionless time

Fig. 14 Average temperature and pressure results obtained with different boundary conditions and an averaging time window size $\Delta = \theta_{max}/4$, with $\theta_{max} = 24$

to break the chemical bonds. For this reason, it would be meaningless to continue the simulation after this time with the adiabatic boundary condition since the chosen physical model would no more be suitable to describe the flow field in this temperature range.

A completely different behaviour is observed for the isothermal wall boundary condition for which the wall temperature is set to the environment temperature (Tw=300 K). In this case, the temperature signal generated by the numerical probe remains limited and close to the environment temperature: even the amplitude of the oscillations is very small and this is due to the fact that the numerical probe is located very close to the solid wall on which the temperature is fixed. Also this boundary condition is not realistic because it represents a perfectly cooled wall which is able to absorb all the thermal power generated inside the cavity. For this reason, also the simulation with this boundary condition is stopped at $\theta = 24$.

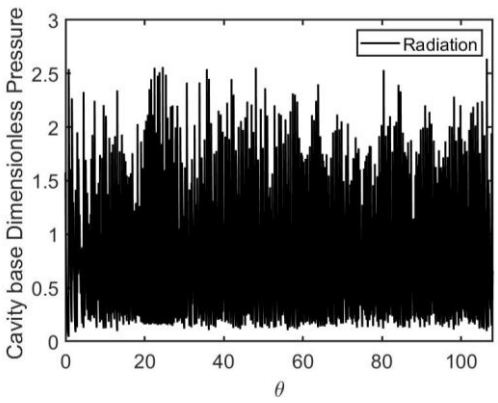

(a) Cavity base dimensionless pressure as a function of dimensionless time

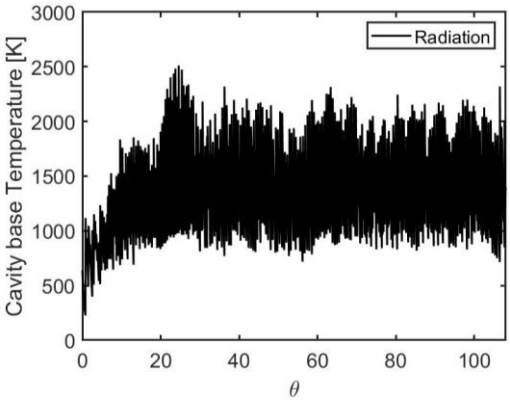

(b) Cavity base temperature as a function of dimensionless time

Fig. 15 Results for the radiating wall boundary condition until $\theta = 107$

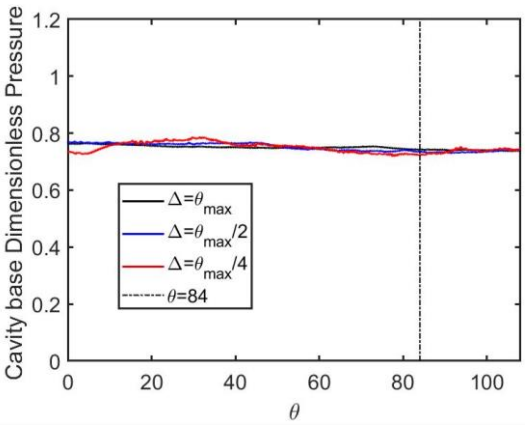

(a) Average cavity base dimensionless pressure as a function of dimensionless time

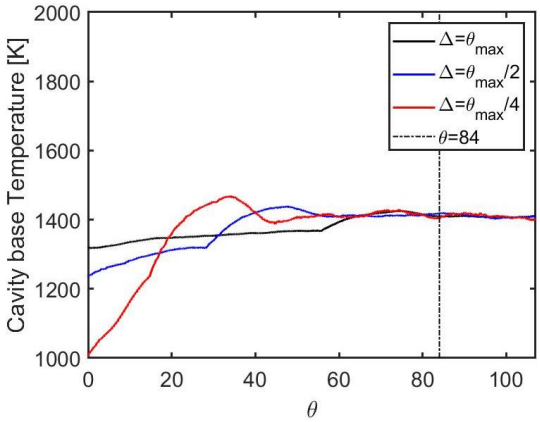

(b) Average cavity base temperature as a function of the dimensionless time

Fig. 16 Results obtained with radiating wall boundary condition and averaging time window sizes $\Delta = \theta_{max},\ \theta_{max}/2,\ \theta_{max}/4$, with $\theta_{max} = 107$

Finally, the plot shows also the results obtained by the radiating wall boundary condition. These results are quite interesting since they show a significant temperature growth without reaching the diverging behaviour observed in the presence of the adiabatic wall boundary condition. For this reason, the use of this boundary condition is further investigated by running the simulation for a larger time interval (until θ =107). The time history of the pressure and temperature for this last simulation are reported in Fig. 15. The averaged results obtained by a moving average with different values of the window size and a final time $\theta_{max} = 107$ are reported in Fig. 16 which shows that both the averaged temperature and pressure reach an asymptotic behaviour.

These results are then compared with the available experimental results provided by Bauer *et al.* (2014) and obtained by a microphone which measured the pressure oscillations. In particular, the experimental pressure spectrum obtained by Bauer *et al.* (2014) is compared with the spectrum obtained by the present numerical results. The spectrum is computed on the pressure signal

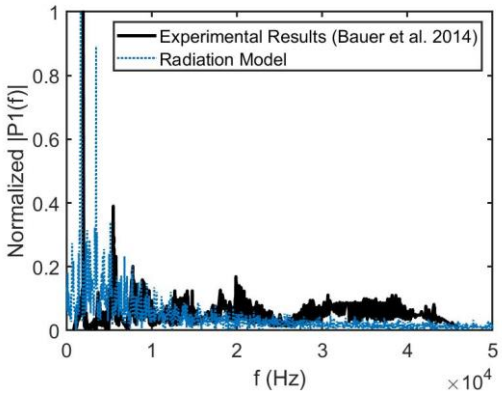

(a) Frequency spectrum

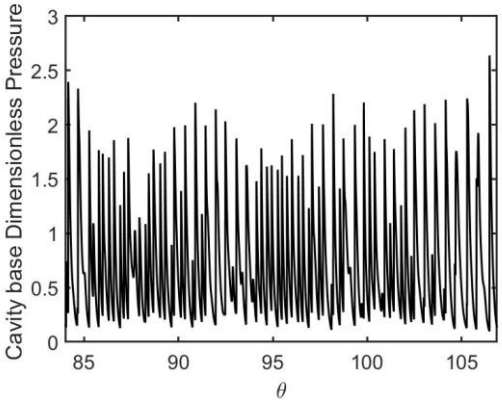

(b) Cavity base dimensionless pressure as a function of dimensionless time

Fig. 17 Frequency spectrum and correspondent cavity base dimensionless pressure for $84 < \theta < 107$. Experimental spectrum derived from the work of Bauer *et al.* (2014)

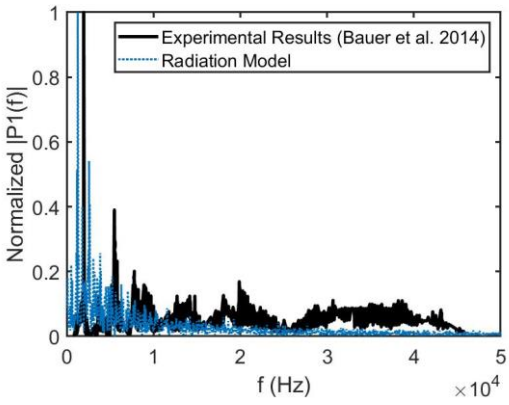

(a) Frequency spectrum

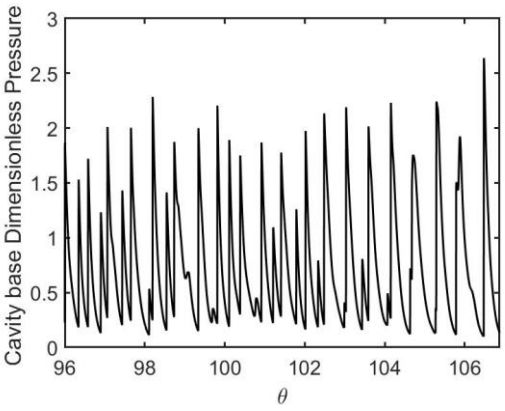

(b) Cavity base dimensionless pressure as a function of dimensionless time

Fig. 18 Frequency spectrum and correspondent cavity base dimensionless pressure for $96 < \theta < 107$. Experimental spectrum derived from the work of Bauer *et al.* (2014)

without considering the initial transient. Different time windows are evaluated for computing the spectrum in order to understand the dependency of the results from the choice of the time window. In particular, the ranges $84 < \theta < 107$ and $96 < \theta < 107$ are considered and the corresponding spectrum is reported in Figs. 17 and 18, respectively. Both results show a peak close to the first experimental peak ($f = 1963$ Hz) but there are noticeable differences between the higher frequency peaks obtained by the numerical simulations and the measured values. One of the possible reasons which could explain these differences could be related to the fact that the experimental spectrum was obtained by measuring the signal with a microphone placed outside the cavity while the numerical results obtained in the present work are referred to the pressure signal evaluated in the cavity. Furthermore, in this work an unsteady RANS approach is used: this means

that only the largest scales are directly solved by the simulation while the fluctuations related to the higher frequencies are not captured but are modelled in the eddy viscosity term.

As far as the average temperature is considered, the present simulation with the radiating boundary condition gives a temperature increase with respect to the environment temperature $\Delta T = 1080$ K, which is comparable with the experimental value $\Delta T \cong 710$ K reported by Bauer *et al.* (2014). The difference between these values can be related to the fact that in the present work the temperature inside the cavity is evaluated while in the experimental setup the temperature was evaluated by a thermocouple applied on the external wall of the resonator. Furthermore, the present simulation does not take into account the axial heat flux across the wall of the cavity which transfer thermal energy from the end to the inlet of the cavity: this leads to an overestimation of the temperature in the numerical simulation. Finally, the physical model used in this work is based on some simplifications (RANS closure model, ideal gas with constant properties,…) which introduce a modelling uncertainty in the results.

5. Conclusions

The flow field inside a resonance igniter was investigated by means of unsteady RANS simulations. After a first grid refinement study, the performance of the igniter were investigated for different thermal boundary conditions applied to the cavity wall. This investigation is motivated by two main reasons. First of all, the test case chosen for this study is based on the experimental work performed by Bauer *et al.* (2014) which is used for validation purposes. However, the experimental results do not include the cavity wall temperature distribution or the wall flux distribution and so the thermal boundary condition is unknown. For this reason, it is necessary to quantify the sensitivity of the results with respect to thermal boundary condition which is generally unknown in this application. In particular, the adiabatic wall boundary condition and the isothermal wall boundary condition (with a constant temperature distribution equal to the environment temperature) represent the extremes of the possible range in which the actual boundary condition is included. A further test is also performed by evaluating the effect of a radiative boundary condition which is applied assuming that the temperature distribution across the thickness of the cavity wall is constant.

The second goal of the present work is to obtain some guidelines which can be exploited to develop resonant igniters with better performances. In particular, the analysis showed that the influence of the boundary condition is so strong that it can change the order of magnitude of the cavity base temperature. These results can be exploited to design an insulating coating on the cavity wall or in the cavity base region.

The simulations presented in this work are affected by several uncertainties related to RANS modelling and fluid modelling. In particular, an ideal fluid with constant specific heats is considered. This hypothesis could lead to an overestimation of the cavity base temperature: if a real fluid is heated up to the temperatures observed in a resonant igniter then the molecules start to dissociate. This means that, when high temperatures are reached, part of the heat trapped in the cavity is used to break chemical bonds instead of inducing a temperature rise. Since this mechanism is missing in an ideal fluid, the numerically predicted cavity base temperature can be overestimated.

In this perspective the present study is presented in the same spirit of a stability analysis of a non-linear dynamic system by means of a simplified (linearized) model: as the linear model can be

used to identify the conditions which trigger the instability but cannot be used to describe the system far from the linearization point, the simplified physical model used in this paper can be used to identify the working conditions which trigger the temperature growth but it cannot be applied to determine the exact asymptotic value of the mean cavity base temperature.

Future work can be devoted to the definition of a conjugate heat transfer problem which involves the solution of the heat equation across the cavity wall in order to quantify the radial and axial heat fluxes inside the solid.

Acknowledgments

Computational resources were provided by HPC@POLITO, a project of Academic Computing within the Department of Control and Computer Engineering at the Politecnico di Torino (http://www.hpc.polito.it).

References

Ampellio, E., Bertini, F., Ferrero, A., Larocca, F. and Vassio, L. (2016), "Turbomachinery design by a swarm-based optimization method coupled with a CFD solver", *Adv. Aircraft Spacecraft Sci.*, **3**(2), 149-170. https://doi.org/10.12989/aas.2016.3.2.149.

Balay, S., Abhyankar, S., Adams, M., Brown, J., Brune, P., Buschelman, K., Dalcin, L., Dener, A., Eijkhout, V., Gropp, W., Karpeyev, D., Knepley, M., Curfman McInnes, L., Mills, R., Munson, T., Rupp, K., Sanan, P., Smith, B., Zampini, S., Zhang, H. and Zhang, H. (2019), Portable, Extensible Toolkit for Scientific Computation, PETSc Users Manual, https://www.mcs.anl.gov/petsc.

Barth, T. and Jespersen, D. (1989), "The design and application of upwind schemes on unstructured meshes", *Proceedings of the 27th Aerospace Sciences Meeting*, Reno, Nevada, U.S.A., January.

Bassi, F., Cecchi, F., Franchina, N., Rebay, S. and Savini, M. (2011), "High-order discontinuous Galerkin computation of axisymmetric transonic flows in safety relief valves", *Comput. Fluids*, **49**(1), 203-213. https://doi.org/10.1016/j.compfluid.2011.05.015.

Bauer, C. and Haidn, O. (2014), "Numerical and experimental investigations on resonance ignition", *Proceedings of the Space Propulsion Conference*, Cologne, Germany, May.

Bauer, C., Lungu, P. and Haidn, O.J. (2019), "Numerical investigation of a resonance ignition system", *Proceedings of the 8th European Conference for Aeronautics and Space Sciences*, Madrid, Spain, July.

Brocher, E. and Ardissone, J. (1983), "Heating characteristics of a new type of Hartmann-Sprenger tube", *Int. J. Heat Fluid Flow*, **4**(2), 97-102. https://doi.org/10.1016/0142-727X(83)90008-5.

Conte, A., Ferrero, A., Larocca, F. and Pastrone, D. (2019), "Numerical tool optimization for advanced rocket nozzle performance prediction", *Proceedings of the AIAA Propulsion and Energy 2019 Forum*, Indianapolis, Indiana, U.S.A., August.

ECHA (2011a), Inclusion of Substances of Very High Concern in the Candidate List, Helsinki, Finland. https://echa.europa.eu.

ECHA (2011b), Proposal for identification of a substance as a category 1A or 1B CMR, PBT, vPvB or a substance of an equivalent level of concern, https://echa.europa.eu.

Ferrero, A. and Larocca, F. (2016), "Feedback filtering in discontinuous Galerkin methods for Euler equations", *Prog. Comput. Fluid Dy.*, **16**(1), 14-25. https://doi.org/10.1504/PCFD.2016.074221.

Ferrero, A. and Larocca, F. (2017), "Adaptive CFD schemes for aerospace propulsion", *J. Phys. Conf. Ser.*, **841**(1), 012017.

Ferrero, A., Iollo, A. and Larocca, F. (2019), "Reduced order modelling for turbomachinery shape design", *Int. J. Comput. Fluid D.*, **34**(2), 127-138. https://doi.org/10.1080/10618562.2019.1691722.

Ferrero, A., Larocca, F. and Bernaschek, V. (2017), "Unstructured discretisation of a non-local transition model for turbomachinery flows", *Adv. Aircraft Spacecraft Sci.*, **4**(5), 555-571. https://doi.org/10.12989/aas.2017.4.5.555.

Frenken, G., Vermeulen, E., Bouquet, F. and Sanders, B. (2002), "Development Status of the Ignition System for Vinci", *Proceedings of the 38th AIAA/ASME/SAE/ASEE Joint Propulsion Conference & Exhibit*, Indianapolis, Indiana, U.S.A., July.

Geuzaine, C. and Remacle, J.F. (2009), "Gmsh: A 3-D finite element mesh generator with built-in pre-and post-processing facilities", *Int. J. Numer. Meth. Eng.*, **79**(11), 1309-1331. https://doi.org/10.1002/nme.2579.

Hartmann, J. (1922), "On a new method for the generation of sound-waves", *Phys. Rev.*, **20**(6), 719. https://doi.org/10.1103/PhysRev.20.719.

Lange, M., Knepley, M.G. and Gorman, G.J. (2015), "Flexible, scalable mesh and data management using PETSc DMPlex", *Proceedings of the 3rd International Conference on Exascale Applications and Software*, Edinburgh, U.K., April.

Lee, J., Lim, D., Seo, S. and Kang, S.H. (2018), "Numerical analysis of the thermal characteristics of a gas-dynamic ignition system", *J. Mech. Sci. Technol.*, **32**(5), 2385-2390. https://doi.org/10.1007/s12206-018-0450-z.

Niwa, M., Santana, A. and Kessaev, K. (2001). "Development of a resonance igniter for GO/kerosene ignition", *J. Propul. Power*, **17**(5), 995-997, https://doi.org/10.2514/2.5860.

Nufer B. (2010), "A Summary of NASA and USAF hypergolic propellant related spills and fires", *Proceedings of the SpaceOps 2010 Conference*, Huntsville, Alabama, U.S.A., April.

Remacle, J.F., Henrotte, F., Carrier-Baudouin, T., Béchet, E., Marchandise, E., Geuzaine, C. and Mouton, T. (2013), "A frontal delaunay quad mesh generator using the l∞ norm", *Int. J. Numer. Meth. Eng.*, **94**(5), 494-512. https://doi.org/10.1002/nme.4458.

Schmidt, J., Hauser, M., Bauer, C. and Haidn, O.J. (2015), "Investigation of stabilization effects in Hartmann-Sprenger-tubes", *Proceedings of the 30th International Symposium on Space Technology and Science (ISTS)*, Kobe, Japan, June.

Song, Y.N., Yu, N.J., Zhang, G.Z., Bin, M.A., Zhou, W.L. and Huang, X. (2005), "Investigation of novel hydrogen/oxygen thruster for orbital maneuver in space station", *Chin. J. Aeronaut.*, **18**(4), 289-294. https://doi.org/10.1016/S1000-9361(11)60247-1.

Spalart, P.R. and Allmaras, S.R. (1994), "A one-equation turbulence model for aerodynamic flows", *Recherche Aerospatiale*, **1**, 5-21, https://doi.org/10.2514/6.1992-439.

Sprenger, H. (1954), "Über thermische Effekte in Resonanzrohren", *Mitteilungen aus dem Institut für Aerodynamik an der ETH Zürich*, **21**, 18.

Stabinsky, L. (1973), "Analytical and experimental study of resonance ignition tubes", NASA-CR-136934, R-9403, NASA, U.S.A.

CC